ARTICLE

Dissociative ionization and electron beam induced deposition of Tetrakis(dimethylamino)silane, a precursor for silicon nitride deposition

Received 00th January 20xx,
Accepted 00th January 20xx

DOI: 10.1039/x0xx00000x

Po-Yuan Shih,*[a,c] Reza Tafrishi,*[b] Maicol Cipriani,[b] Christian Felix Hermanns,[a] Jens Oster,[a] Armin Gölzhäuser,[c] Klaus Edinger[a] and Oddur Ingólfsson **[b]

Motivated by the use of tetrakis(dimethylamino)silane (TKDMAS) to produce silicon nitride-based deposits and its potential as a precursor for Focused Electron Beam Induced Deposition (FEBID), we have studied its reactivity towards low energy electrons in the gas phase and the composition of its deposits created by FEBID. While no negative ion formation was observed through dissociative electron attachment (DEA), significant fragmentation was observed in dissociative ionization (DI). Appearance energies (AEs) of fragments formed in DI were measured and are compared to the respective threshold energies calculated at the DFT and coupled cluster (CC) levels of theory. The average carbon and nitrogen loss per DI incident is calculated and compared to its deposit composition in FEBID. We find that hydrogen transfer reactions and new bond formations play a significant role in the DI of TKDMAS. Surprisingly, a significantly lower nitrogen content is observed in the deposits than is to be expected from the DI experiments. Furthermore, a post treatment protocol using water vapour during electron exposure was developed to remove the unwanted carbon content of FEBIDs created from TKDMAS. For comparison, these were also applied to FEBID deposits formed with tetraethyl orthosilicate (TEOS). In contrast, effective carbon removal was achieved in post treatment of TKDMAS. This approach only marginally affected the composition of deposits made with TEOS.

Introduction

Silicon nitride (SiN_x) thin films are dielectric materials that play an important role in the semiconductor industry. By varying the Silicon/Nitrogen composition or deposition methods, such films can serve as passivation layers in device packaging,[1,2] insulators of interconnects in Back End of Line (BEOL),[3] gate spacers for high mobility channel transistor fabrication[4] and more.[5] Silicon oxynitrides (SiO_xN_y) are also essential materials in the semiconductor industry[6] as a dielectric layer and for integrated optics and waveguides.[7]

Currently, the leading thin film deposition techniques, besides plasma-based processing, are chemical vapour deposition (CVD)[8] and atomic layer deposition (ALD).[8,9] Correspondingly, gas phase precursors are adapted for the intended deposit and the applied method. Focused electron beam induced deposition (FEBID)[10–13] is an alternative deposition approach suited for a single step layer deposition of well-defined spatial dimensions in the nm-regime as well as for the deposition of three-dimensional nanostructures.[14] From the fundamental physical and chemical point of view, the main difference between these approaches is that CVD (and thermal ALD) are thermally driven processes, while FEBID is electron driven. Tetrakis(dimethylamino)silane (TKDMAS) was initially introduced as a CVD precursor,[15] shows promising characteristics such as high deposition rate and low temperature requirements and has also been shown to perform well in ALD.[16]

Unlike the thermally driven CVD, FEBID attracts the spotlights from industry[17] due to its low temperature, single step, and mask-free patterning capability. In FEBID, a high energy focused electron beam is directed at a substrate's surface in the presence of a continuous supply of precursor gas. The set-up is commonly a scanning electron microscope (SEM) with an additional gas injection systems (GIS)[13,18–20] coupled to a fine capillary for precursor delivery near to the electron beam impact side. The precursor molecules decompose under the focal area of the primary beam, but also outside that area within the extent of the back-scattered electrons (or scattered electrons in general when 3-D deposits are generated). The deposit then forms from the non-volatile fragments

[a] *Carl Zeiss SMT GmbH, Industriestraße 1, 64380 Roßdorf, Germany.*
[b] *Science Institute and Department of Chemistry, University of Iceland, Dunhagi 3, 107 Reykjavik, Iceland.*
[c] *Faculty of Physics, Bielefeld University, 33615 Bielefeld, Germany.*
† * Equal First author contribution
** Corresponding author
Electronic Supplementary Information (ESI) available: [details of any supplementary information available should be included here]. See DOI: 10.1039/x0xx00000x

Please do not adjust margins

while the volatiles are pumped away. In this decomposition process, secondary electrons generated through the primary and scattered electrons are generated and play a determining role.[21,22] The energy distribution of these secondary electrons generally peaks around or below 10 eV and is appreciable close to 0 eV.[23,24] Towards higher energies, it falls fairly rapidly but has a long tail. Somewhat arbitrarily, the SEs are defined as low energy electrons in the energy range from 0 - 50 eV or 0 - 100 eV. Notwithstanding, the decomposition processes of the precursor, subjected to these electrons, can be categorized into four distinct mechanisms; dissociative ionization (DI), dissociative electron attachment (DEA), neutral dissociation (ND), and dipolar dissociation (DD)[25]. These are distinctly different processes, with different energy dependence and, most importantly, different product (fragment) formation leading to different fragment composition and reactivity. The extent of the individual processes is thus expected to critically influence the deposition process and the composition of the deposit in FEBID.

Considering the expectation of broader applications being fulfilled by expanding the deposition methods of SiN_X and SiN_xO_y, we are interested in searching for precursor candidates and design paths for FEBID and thus exploring the extent and nature of low energy electron induced decomposition of such precursors. In that context, we have studied the reactivity of TKDMAS concerning dissociative electron attachment and dissociative ionization in the gas phase under single collision conditions and the elemental composition of deposits made in FEBID of this precursor as well as ex-situ post deposition purification through electron irradiation in the presence of water. For comparison, the same post-deposition protocol was applied to Tetraethylorthosilicate (TEOS), a silicon-based precursor used for deposition of glue layers for adhesion of low-k material in the wafer production[26,27] -a precursor that has been used in CVD[28–30] as well as in FEBID.[31,32]

While DI is an efficient process, we did not detect any DEA products from TKDMAS within the sensitivity of our instrument. Here we thus focus on the DI process. We have determined the experimental appearance energies for the main fragments formed, and to aid our interpretation of the DI processes, we have calculated the respective threshold energies at the DFT and the coupled cluster level of theory. Further, the average carbon and nitrogen loss per incident is calculated by taking the sum of all the main fragment contributions, weighted by the respective carbon and nitrogen losses, and dividing that by the total intensity of all fragmentation events. This average carbon and nitrogen loss is compared to the elemental composition of FEBID deposits as determined by energy-dispersive x-ray (EDX) spectroscopy and further discussed in context to the composition change observed in post-deposition electron exposure in the presence of water.

Methods

Gas phase studies

Mass spectra and ion yields of TKDMAS were studied with an electron-molecule crossed beam setup described in detail previously.[33] Here, only a brief description of the experiments will be given. The instrument is under a high vacuum with the base pressure in the range of 10^{-8} mbar. It consists of a trochoidal electron monochromator (TEM), gas inlet system equipped with a leak valve, and a quadrupole mass spectrometer (Hiden EPIC1000). A quasi mono-energetic beam is generated with the trochoidal electron monochromator and crosses an effusive molecular beam in the interaction area that is defined by the extraction optics of the mass spectrometer. The ions formed are extracted in a week electric field and focused into the QMS. Both positive and negatively charged ions can be monitored by changing the polarity of the respective electric optics. During experiments, an effusive beam of TKDMAS was evaporated to the reaction zone at room temperature, and during measurements, the pressure was kept constant at approximately 1 x 10^{-6} mbar using the leak valve. To avoid deposition of the target gas on the electrical lens components, the monochromator is kept at 120 °C using two halogen lamps. Mass spectra are recorded at fixed electron energies by scanning through the relevant m/z range, and ion yield curves are recorded at fixed m/z by scanning through the relevant energy range.

For positive ion yields, the electron energy was calibrated using the onset of the Ar^+ signal from Ar, and for determination of the appearance energies (AEs), the onsets of the ion yields were fitted with a Wannier type function of the form:

$$E \leq AE,\ f(x) = b$$

$$E > AE,\ f(x) = b + a\,(E - AE)^{d}$$

Here, E refers to the energy of the incident electrons, AE refers to the appearance energy, b is a constant accounting for the background signal, a is a scaling coefficient, and d is an exponential factor. The ion yield curves for each fragment were obtained from the average of multiple scans recorded on different days. The standard deviations of the fitted averaged scans were found to be between 0.2 eV - 0.4 eV.

Deposition and EDX analysis

Focused electron beam induced deposition and energy-dispersive X-ray analyses were performed with a Zeiss photomask repair tool MeRiT® and an Oxford Instruments EDX detector integrated Zeiss Crossbeam system, respectively. FEBIDs and EDX analysis were carried out at room temperature. The substrate was a 4 inch-silicon wafer coated with a 100 nm thick polycrystalline gold film purchased from Georg Albert PVD. It was chosen because the EDX peak of Au is distinguishable from the Si, N, and C deposits. Measurements were carried out at 5 keV primary beam energy. For the FEBIDs presented here, an electron dose of 2.51×10^{14} e^-/cm^2 and 3.94×10^{14} e^-/cm^2 was applied on a scanning area of 1 μm^2 using the precursor TKDMAS and tetraethyl orthosilicate (TEOS),

This journal is © The Royal Society of Chemistry 20xx

Please do not adjust margins

Please do not adjust margins

respectively. SEM images were obtained from a Zeiss photomask repair tool MeRiT®, and the topographic images were obtained from a Brucker AFM tool Dimension Icon®. A typical preparation and analysis cycle included initial FEBID in a MeRiT® instrument and transfer for AFM and EDX measurements. SEM imaging and post deposition purification was then conducted in a second MeRiT® instrument before post deposition purification transfer for AFM and EDX measurements. Reproducible results were obtained for several repeats. Tetrakis(dimethylamino)silane (TKDMAS) was purchased from Gelest, USA, with stated purity of 99% for both deposition and gas phase experiments. Tetraethyl orthosilicate (TEOS) was purchased from Merck, Germany. Both were used as delivered without further purification.

Quantum chemical calculations

All calculations were performed using the ab initio quantum chemistry program package ORCA.[34] Geometry optimizations were carried out with density functional theory (DFT) using PBE0,[35] a hybrid general gradient approximation (GGA) based on the Perdew–Burke-Ernzerhof (PBE) functional. The basis set used was the valence triple-zeta polarization basis set def2-TZVP.[36] In addition, the D3(BJ) dispersion correction by Grimme et al.[37] was included. We used the restricted Kohn-Sham (RKS) formalism for closed-shell systems and the unrestricted (UKS) for open-shell systems. Harmonic vibrational frequencies were calculated at the same level of theory and were confirmed to be positive. They were then used to derive the zero-point energies and the thermal energy corrections at 298 K for the neutral parent molecule and all the fragments. Coupled cluster calculations were performed on optimized geometries using domain-based local pair natural orbitals with single, double, and perturbative triple excitations, DLPNO-CCSD(T).[38–40] This was done with a tight PNO setting, using DZ/TZ extrapolation with the split valence polarization basis set def2-SVP[36], the valence triple-zeta polarization basis set def2-TZVP, and the auxiliary valence quadruple-zeta basis set with two sets of polarization functions, def2-QZVPP/C.[41]

All threshold calculations, both at the DFT and DLPNO-CCSD(T) level of theory, were carried out using the single point energies of the relaxed structures and were obtained by subtracting the total energy of all fragments formed in the respective processes from the total energy of the parent molecule. In all cases, the respective ZPVEs and thermal energy corrections were included.

Results and discussion

Figure 1a shows a positive ion mass spectrum resulting from 50 eV electron impact ionization and dissociation of TKDMAS under single collision conditions in the gas phase. The mass spectrum is recorded in the m/z range from about 10 to 210 and is characterized by a significant contribution from the parent ion and the loss of 1, 2, and 3 neutral $N(CH_3)_2$ units. These appear at the m/z ratios 204; $Si(N(CH_3)_2)_4^+$, 160; $Si(N(CH_3)_2)_3^+$, 116; $Si(N(CH_3)_2)_2^+$ and 72; $SiN(CH_3)_2^+$, respectively. In addition, significant contributions are observed at m/z 117, 74, 45, and 44 as can be seen in the expanded section of the mass spectrum shown in figure 1b. We attribute the m/z 117 contribution to $HSi(N(CH_3)_2)_2^+$, i.e., hydrogen transfer from one of the two dissociated $N(CH_3)_2$ fragments to the remaining m/z 116 moiety ($Si(N(CH_3)_2)_2^+$). For the m/z ratios 45 and 44, however, we observe significant changes in the relative signal intensity, as compared to the molecular cation, between mass spectra. The contributions from these fragments are most significant with freshly loaded samples but diminish as the measurement time progresses.

The synthesis of $Si(N(CH_3)_2)_4$ is based on the reaction of dimethylamine, $HN(CH_3)_2$, with silicon tetrachloride, and we anticipate that the high m/z 45 and 44 signals, when the sample is freshly loaded is partly due to residual dimethylamine in the sample and that this is reflected in the AEs determined for these fragments. This is discussed further here below. The m/z 74 contribution also shows this behaviour, though to a lesser extent, which may also in part be due to impurities when the sample is freshly loaded. However, we attribute the bulk of the m/z 74 contribution to the formation of the trimethylhydrazin cation; $(H_3C)_2N\text{-}NH(CH_3)^+$, as is discussed here below. Minor contributions corresponding to further methane, methyl, or methylene loss from the main fragments are also observed in the mass spectrum, i.e., at m/z 144, 131, 101, and 86. Below m/z, 44 minor contributions are observed at around m/z

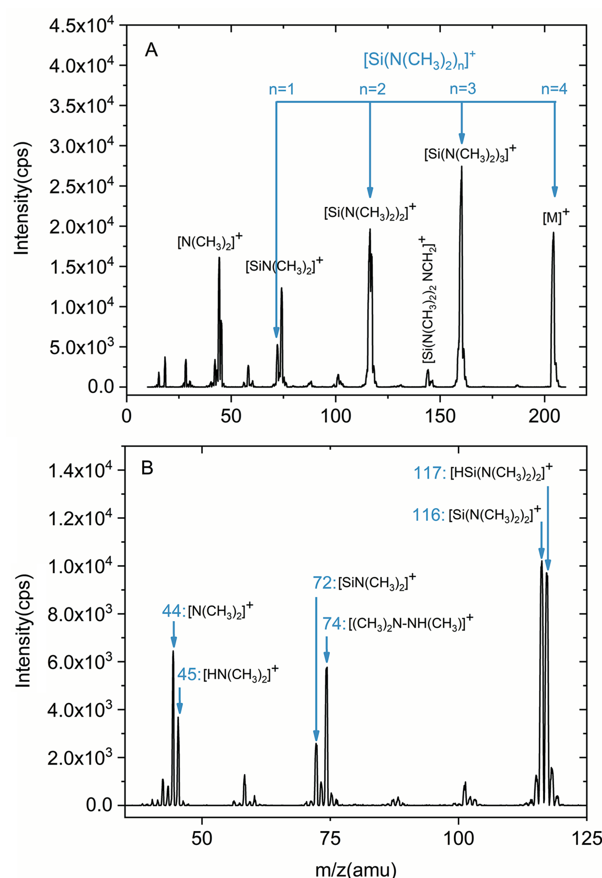

Figure 1. A) Electron impact ionization mass spectrum of TKDMAS recorded at 50 eV incident electron energy. B) high-resolution expansion of the m/z range from about 30 to 125.

Please do not adjust margins

42, 28, 18, and 15. These stem from residual nitrogen, water, and pump oil always present in HV experiments, though m/z 15 may also be in part due to CH_3^+ from TKDMAS.

Figure 2 shows the ion yield curves for the main fragments observed over the energy range from below the ionization energy of TKDMAS up to about 50 eV. The ion yields were normalized to the pressure and the signal intensity of Ar^+ at 50 eV incident electron energy measured separately at the beginning and end of every measurement day:

$$I_{norm} = \left(\frac{I_{m/z}}{I_{Ar}}\right)\left(\frac{P_{Ar}}{P_{m/z}}\right)$$

Here $I_{m/z}$ and $P_{m/z}$ are the intensities and pressures of the particular fragments, respectively, and I_{Ar} and P_{Ar} those of Ar^+. Table 1 shows the relative intensities of individual contributions calculated from the peak heights in the mass spectra shown in figure 1 (recorded at 50 eV impact energy) and from the area under the ion yield curves shown in figure 2 (from the respective onsets up to 50 eV). In both cases, the intensities are normalized to the m/z 160, which is set as 100. At the bottom of table 1, the average carbon and nitrogen loss per incident is also shown, derived by taking the sum of all the main fragment contributions weighted by the respective carbon and nitrogen losses and dividing that by the total intensity of all ionization events. For example, the m/z ratio 160 represents the loss of an $N(CH_3)_2$ unit, which in turn corresponds to the loss of one nitrogen and two carbons. This is weighted proportionally as the contribution of the m/z 160 signal intensity to the average nitrogen and carbon loss per fragmentation incidents. The contributions from m/z 44 are recorded after several days of measurements with the same sample and is weighted as the loss of one $N(CH_3)_2$ unit. Contributions from m/z 45 are not considered.

The ion yield curves in figure 2, show the typical non-resonant profile of electron impact ionization and dissociation with an onset region reflecting the threshold of the individual processes and a plateau at higher energies. The onset slope of the molecular ion is fairly steep compared to that of the fragmentation products, as it is mainly defined by increasing intensity loss into the respective fragmentation channels with increasing excess energy. For the more extensive, metastable fragmentation channels, where internal energy redistribution is important, the excess energy plays an increasing role, and the onset slopes become shallower. This also becomes more apparent as the fragmentation becomes more extensive. Noticeably, in table 1, the relative integral intensity of the parent ion from the ion yield curves is higher than the peak intensity in the mass spectrum. This is mainly a reflection of the higher threshold for the fragmentation processes. However, different voltages on the electrical lens components (mainly the extraction and entrance components to the QMS) may also influence the detection efficiency of the individual fragments differently. This is reflected in the slightly lower average carbon and nitrogen loss per incident, as determined from the ion yields compared to those from the mass spectra. However, the overall picture is the same, and the average C:N loss ratio is in both cases 2, reflecting the dominating loss of $N(CH_3)_2$ units.

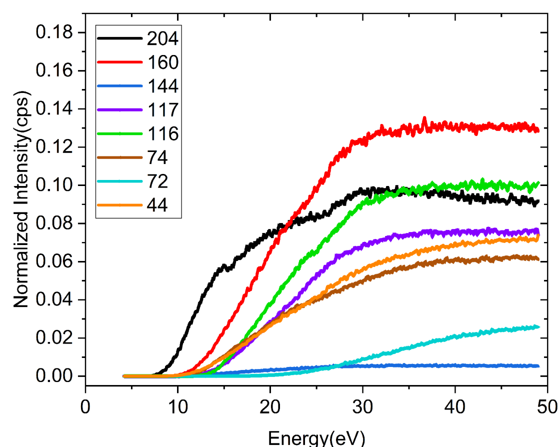

Figure 2. Positive ion yield curves for the main fragments observed in dissociative ionization of TKDMAS in the electron energy range from about 0-50 eV. The ion yields were normalized to the pressure and the signal intensity of Ar^+ from Ar at 50 eV incident electron energy.

Table 2 shows the appearance energies of the individual fragments determined by fitting a Wannier type threshold function to the onset of the individual ion yield curves as described in the experimental section. The confidence limits are set to clearly bracket the onset concerning the average value determined from the respective curves. These are equal to or higher than the standard deviations from the fittings and are judged by visual inspection of individual curves. Representative fits to the ion yield of the parent ion and that for the loss of 1, 2, and 3 $N(CH_3)_2$ units are shown in figure 3 with the respective average AEs and confidence limits. Table 2 also shows the thermochemical thresholds for the individual processes calculated at the PBE0/def2-TZVP (DFT) and the DLPNO-CCSD(T)/Extrapolate (2/3, def2) (coupled cluster; CC) level of theory. Where an agreement of the AEs with the calculated direct processes is not found to be acceptable, which in fact is the case for most of the fragments, we have computed alternative pathways. The threshold values at the DLPNO-CCSD(T) level of theory, shown in table 2, for the direct fragmentation processes are underlined, and those for the rearrangement reaction that agree best with the AEs are bold. At the bottom of the table, the AEs for the m/z ratio 45 and 44 are shown for measurements with freshly loaded samples. For m/z 45, the AE is compared to the threshold values calculated for the ionization of dimethyl amine (DMA) and the formation of the DMA cation from TKDMAS. For m/z 44, the AE is compared to hydrogen loss from the nitrogen and to hydrogen loss from one of the methyl groups of DMA. The geometries of all fragment ions, optimized at the coupled cluster level of theory are shown in figure 4.

This journal is © The Royal Society of Chemistry 20xx

Please do not adjust margins

Table 1. Relative intensities of individual contributions and the average carbon and nitrogen loss per incident obtained from the mass spectrum and ion yields at 50 eV.

Fragment	m/z	Peak height from mass spectrum	Integration from ion yields
$[M]^+$	204	47.15	85.73
$[Si(N(CH_3)_2)_3]^+$	160	100	100
$[Si(N(CH_3)_2)_2\ NCH_2]^+$	144	7.87	4.30
$[HSi(N(CH_3)_2)_2]^+$	117	60.31	54.34
$[Si(N(CH_3)_2)_2]^+$	116	71.57	71.18
$[(CH_3)_2N–NH(CH_3)]^+$	74	44.93	44.07
$[Si(N(CH_3)_2)]^+$	72	19.20	10.72
$[N(CH_3)_2]^+$	44	58.74	48.50
Average nitrogen loss per incident		1.60	1.40
Average carbon loss per incident		3.20	2.80

The DFT approach results in lower values than the CC approach for all calculated thresholds. The difference is in the range of 0.1 to 0.6 eV and largest for the molecular ion. The AE of the molecular ion, i.e., the ionization energy of TKDMAS, is found to be 7.6 ± 0.2 eV, which agrees well with the CC calculations for the threshold (7.58 eV), but is about 0.6 eV higher than the threshold energy calculated at the DFT level of theory. For the loss of one $N(CH_3)_2$ unit, we determine an AE of 9.6 ± 0.2 eV, which is about 0.4 eV higher than the CC threshold value. Direct dissociation is the lowest energy process in this case, and we do not expect significant barriers. However, it is not uncommon, especially in metastable decay processes, that electron impact studies slightly overestimate the respective thresholds as excess internal energy may be needed for dissociation to be observable on the timescale of the respective experiment. This effect is commonly referred to as "kinetic shift". For the loss of 2 $N(CH_3)_2$ units (m/z 116), on the other hand, we find our experimental AEs to be more than 2 eV below the computed CC threshold value, i.e., 12.1 ± 0.2 eV as compared to 14.03 eV. This is way outside the confidence limits of our measurements and the accuracy of either the DFT or CC calculations, indicating that a lower energy rearrangement process is operative at the threshold. The only process offering significant energy gain in this reaction is the combination of the two neutral $N(CH_3)_2$ units to form $(H_3C)_2N–N(CH_3)_2$, tetramethylhydrazine. We calculate a threshold of 11.48 eV and 11.80 eV for this process at the DFT and CC level of theory, respectively. From these, the CC threshold value agrees well with our experimental AE supporting the notation that this process is not direct but associated with a new NN bond formation at the threshold. Similarly, we find the AE for the loss of 3 $N(CH_3)_2$ units, m/z 72, to be about 2 eV below the CC threshold value. Though our accuracy for the AE for this channel is less than for the loss of two $N(CH_3)_2$ units, that cannot explain this difference. However, if we consider the formation of tetramethylhydrazine again, we compute a threshold of 14.27 eV at the coupled cluster level of theory. This is in good agreement with our AE of 14.5 ± 0.2 eV. In addition to the

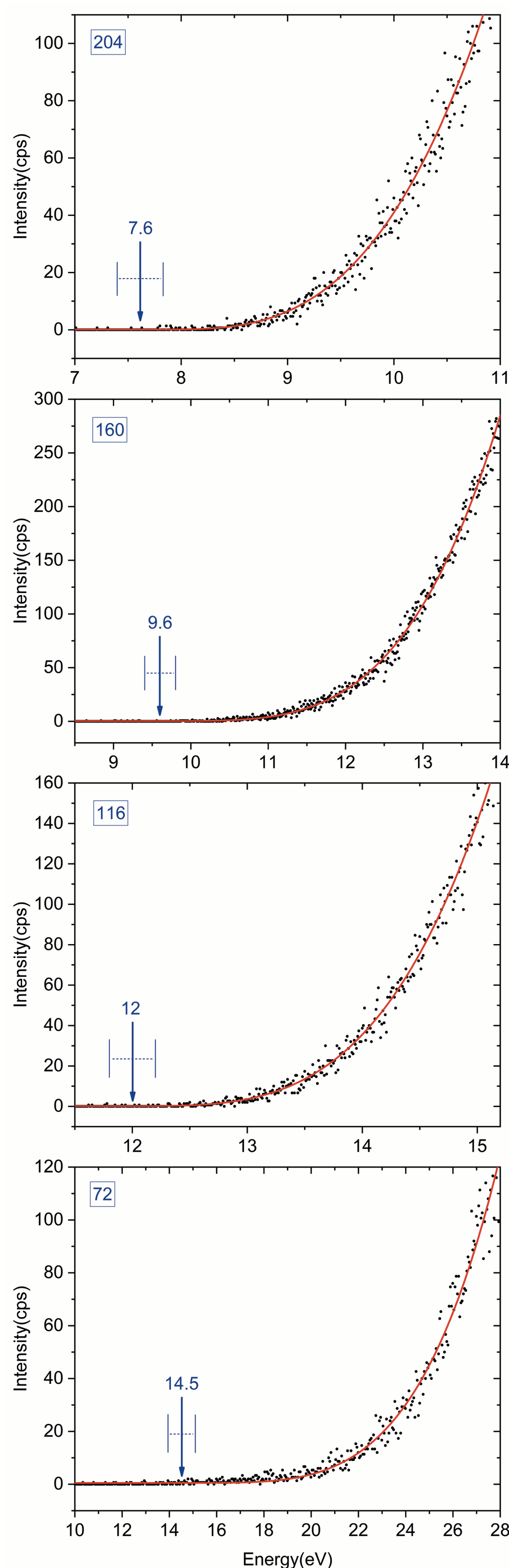

Figure 3. Representative fits to the onset area of the DI ion yields for the parent ion and for the loss of 1, 2 and 3 N(CH3)2 units from TKDMAS. The average AEs and determined from three independent fits are shown along with the respective confidence limits.

Please do not adjust margins

Please do not adjust margins

loss of $N(CH_3)_2$ units, we have also considered fragmentation paths leading to the m/z ratios 144, 117, 74, and 44 from TKDMAS. From these, the m/z ratios 144 is attributed to $N(CH_3)_2$ loss and additional CH_3 and hydrogen loss. For this process, the direct dissociation of these three neutrals results in a threshold of 14.4 eV at the CC level of theory, again more than 2 eV above the 12.1 eV experimental AE. Hydrogen transfer leading to the neutral fragments $HN(CH_3)_2$ or methane, however, results in CC threshold values that are about 1.5 and 2 eV below the AE, respectively. Assuming the formation of trimethylamine; $HN(CH_3)_2$ and the CH_3 radical, on the other hand, results in a CC threshold value of 11.81, in good agreement with the experimental AE. The m/z 117; $HSi(N(CH_3)_2^+)_2$ constitutes a hydrogen transfer from one of the dissociating neutrals to the charge retaining fragment. For this process, we derive an AE of 12.1 ± 0.3 eV, compared to a calculated CC threshold value of 11.41, without considering NN bond formation between the neutrals. The formation of an NN bond brings the CC threshold energy further down, thus further away from the experimental AE. We note that the ion yield for this fragment is bound to contain about 10 % isotope contributions from m/z 116. This is significant as the relative isotope contribution is high, and the intensities are similar for m/z 116 and 117. Thus the threshold behaviour for m/z 117 is likely to be influenced by the m/z 116 contributions. However, the calculated threshold energies for m/z 116 are slightly higher than

Table 2. Appearance energies (AEs) and calculated thresholds for potential DI reactions leading to the fragments observed upon DI of TKDMAS. Threshold values at the DLPNO-CCSD(T) level of theory for the direct fragmentation processes are underlined and those for the rearrangement reactions that agree best with the respective AEs are bold. Additionally, at the bottom of the table, the AEs for the m/z ratio 45 and 44 measured with freshly loaded samples are compared to the threshold values calculated for the ionization of dimethyl amine and the formation of the DMA cation from TKDMAS for m/z 45 and hydrogen loss from the nitrogen and one of the methyl groups for m/z 44, respectively.

Fragment	Product	AE (eV)	PBE0 (eV)	DLPNO-CCSD(T) (eV)
204	M: $Si(N(CH_3)_2)_4^+$	**7.6 ± 0.2**	6.99	**7.58**
160	$[Si(N(CH_3)_2)_3]^+ + N(CH_3)_2$	**9.6 ± 0.2**	8.98	**9.21**
144	$[Si(N(CH_3)_2)_2 NCH_2]^+ + N(CH_3)_3 + H$	**12.1± 0.3**	11.72	**11.81**
	$[Si(N(CH_3)_2)_2 NCH_2]^+ + N(CH_3)_2 + CH_3 + H$		14.27	14.4
	$[Si(N(CH_3))_2 NCH_2]^+ + N(CH_3)_2 + CH_4$		9.93	10.07
	$[Si(N(CH_3)_2)_2 NCH_2]^+ + HN(CH_3)_2 + CH_3$		10.47	
117	$[HSi(N(CH_3)_2)_2]^+ + N(CH_3)(CH_2) + N(CH_3)_2$	12.1± 0.3	11.22	**11.41**
116	$[Si(N(CH_3)_2)_2]^+ + (CH_3)_2N\text{-}N(CH_3)_2$	**12.0± 0.2**	11.48	**11.80**
	$[Si(N(CH_3)_2)_2]^+ + N(CH_3)_2 + N(CH_3)_2$		13.44	14.03
74	$[(CH_3)_2N\text{–}NH(CH_3)]^+ + (CH_2)Si(N(CH_3)_2)_2$	**10.7± 0.2**	10.87	**11.34**
	$[H_2Si(N(CH_3)_2)]^+ + N(CH_2)_2 + 2N(CH_3)_2$		15.75	16.12
	$[H_2Si(N(CH_3)_2)]^+ + N(CH_3)_2 + 2\ N(CH_2)(CH_3)$		13.70	13.79
	$[H_2Si(N(CH_3)_2)]^+ + (CH_3)_2N\text{–}N(CH_3)_2 + N(CH_2)_2$		13.75	13.91
72	$[Si(N(CH_3)_2)]^+ + (CH_3)_2N\text{-}N(CH_3)_2 + N(CH_3)_2$	**14.5± 0.4**	14.12	**14.27**
	$[Si(N(CH_3)_2)]^+ + N(CH_3)_2 + N(CH_3)_2 + N(CH_3)_2$		16.08	16.5
44	$[HN(CH_2)(CH_3)]^+$ (H migration) + $Si(N(CH_3)_2)_3$	**10.4± 0.2**	9.95	**10.26**
	$[N(CH_3)_2]^+ + Si(N(CH_3)_2)_3$		13.25	13.77
45	$HN(CH_3)_2 + e^- \rightarrow [HN(CH_3)_2]^+$ (Ionization energy of DMA)	8.6± 0.2	7.86	8.10
	$Si(N(CH_3)_2)_4 + e^- \rightarrow [HN(CH_3)_2]^+ + Si(N(CH_3)(CH_2)$		11.56	11.92
44	$HN(CH_3)_2 + e^- \rightarrow [HN(CH_2)(CH_3)]^+ + H$	9.75 ± 0.2	9.57	9.54
	$HN(CH_3)_2 + e^- \rightarrow [N(CH_3)_2]^+ + H$		13.54	13.73

This journal is © The Royal Society of Chemistry 20xx

Please do not adjust margins

for m/z 117 and should thus not mask the true m/z 117 onset. There are also no indications of the m/z 117 fragment being from impurities. Thus, we anticipate that the higher AE than the CC calculations reflects activation barriers on this reaction path. This is a reasonable assumption, considering the complexity of this reaction. Still, an alternative explanation may be a kinetic shift, as this channel is likely to proceed on a fairly long-time scale. In principle, the m/z 74 is concord with the formation of $[H_2Si(N(CH_3)_2)]^+$ through the transfer of two hydrogens from the leaving $N(CH_3)_2$ units to the remaining charged Si-containing moiety. For m/z 74, we derive an AE of 10.6 eV as compared to a 16.12 eV CC threshold value for the direct formation of $[H_2Si(N(CH_3)_2)]^+$ with both hydrogen transferred from the same $N(CH_3)_2$ unit. This value is lowered to 13.79 eV by assuming hydrogen transfer from two different $N(CH_3)_2$ units but considering NN bond formation in this process does not bring the threshold further down (see table 2). It is thus clear that m/z 74 does not constitute the formation of $[H_2Si(N(CH_3)_2)]^+$. Considering the formation of the trimethylhyrazine cation; $(CH_3)_2NNH(CH_3)_2^+$, leaving the saturated $H_2C{=}Si(N(CH_3)_2)_2$ neutral counterpart, brings the DFT threshold value down to about 10.87 eV and the CC value down to 11.34 eV. This is in better agreement with the experimental AE, but contributions from impurities cannot be excluded. For m/z 44, we derive an AE of 10.4 ± 0.2 eV from ion yields recorded several days after the fresh sample was loaded. The CC threshold value for the direct dissociation is 13.73 eV; however, considering the formation of the methylamino cation $CH_2{=}NH(CH_3)^+$ results in a CC threshold of 9.54 eV, which is in better agreement with the experimental AE.

For m/z 45 and 44 from dimethyl amine (DMA), we derive CC threshold values of 8.10 eV and 9.54 eV, respectively. The ionization energy of DMA, reported at the NIST Chemistry Webbook[42] are in the range from 8.07 - 9.97 eV with the recommended value being 8.24 ± 0.02 eV. For the ionization energy of DMA, i.e., the AE of m/z 45, we derive a value of 8.6 ± 0.2 eV, which is slightly higher than the CC threshold value and the experimental value recommended at the NIST Chemistry WebBook.

The DI (electron impact) values reported at the NIST Chemistry Webbook[42] for the AE of m/z 44 from DMA range from 9.41 - 10.55 eV. However, a more recent PE study by Traeger report an AE_{298} of 9.69 ± 0.01 eV[43] and TPEPICO measurements by Bodi et al.[44] report an AE_0 of 9.768 ± 0.023 eV. These are slightly higher than the current CC threshold value of 9.54 eV. We note that Bodi et al. derived a 0 K value of 9.749 eV with the W1U composite approach, which shows that the current DLPNO-CCSD(T) approach slightly underestimates the threshold for this process. For the m/z 44 recorded directly after loading a fresh sample, we derive an AE of 9.75 ± 0.2 eV, which is in good agreement with the values reported by Traeger[43] and from Bodi et al.[44]

In recent years several studies have been reported on potential organometallic FEBID precursors. These were subjected to electron induced decomposition under non-steady state UHV conditions and

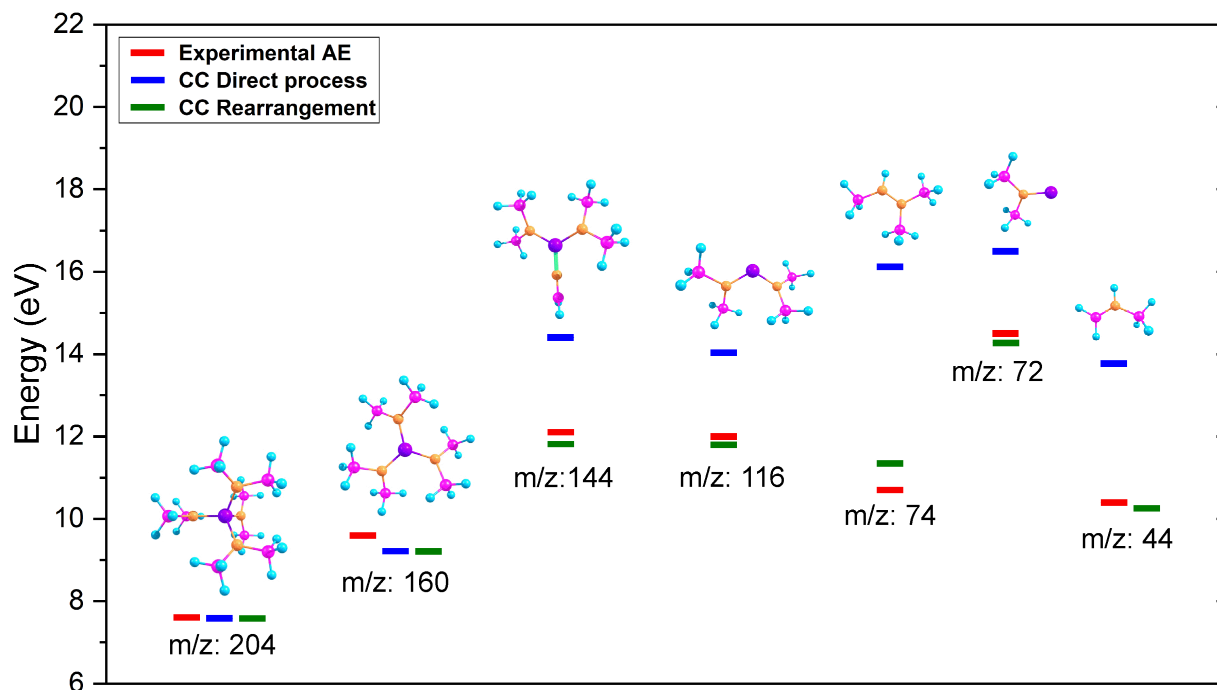

Figure 4. Comparison of the experimentally determined appearance energies and the thresholds calculated for the respective fragments at the coupled cluster level of theory. The experimental appearance energies are shown with red lines and the calculated thresholds for the direct processes without new bond formation are shown with blue lines. These correspond to the underlined values in table 2. The calculated thresholds for the rearrangement processes that agree best with the experimental appearance energies and are formatted bold in table 2 are shown in green. Additionally, the geometries of the respective positive ions optimized at the CC level of theory are shown above the respective AEs and E_{th} values.

Please do not adjust margins

compared with the extent of the fragmentation of these compounds through DEA and DI under single collision conditions.[45–48] In these experiments, 1 - 2 monolayers of the respective precursor were adsorbed on a gold substrate and exposed to 500 eV electron irradiation from a flood gun. Desorbing fragments were monitored by mass spectrometry, while the changes in the adsorbate's composition were monitored by XPS as a function of electron dose. For $Pt(PF_3)_4$,[49] $Ru(CO)_4I_2$,[47] cis-$Pt(CO)_2Cl_2$,[50] $MeCpPtMe_3$,[25] (η^5-Cp)$Fe(CO)_2Re(CO)_5$[46] and $CpFe(CO)_2Mn(CO)_5$[45] an initial fast decomposition step was observed in the range up to about 10^{15} e^-/cm^2 electron dose that led to an average ligand loss of 1-2 per precursor molecule. A much slower decomposition step was observed at higher doses (above ~10^{16} e^-/cm^2), leading to further decomposition of the deposits. In these experiments, the average number of ligands lost in the initial fast decomposition step correlated well with the average number of ligands lost per DEA incident in the gas phase under single collision conditions, indicating that the quick initial decomposition step was governed by DEA rather than DI.[25,47] On the other hand, neutral dissociation has also been shown to be very efficient for $Pt(PF_3)_4$,[49,51,52]. In contrast, it has not been probed for the other precursors mentioned here and in the case of $CpFe(CO)_2Mn(CO)_5$,[45] it was in fact concluded that DI rather than DEA dominated the initial fragmentation step.

Here we take a similar approach as previously taken in comparing the surface science experiments with the respective gas phase experiments. We compare the extent of the DI process as observed under single collision conditions with the elemental composition of FEBID pads created with TKDMAS. Furthermore, post treatment of the FEBID deposits through electron irradiation under water vapour was conducted on the pads in order to reduce the carbon content of the deposits. For comparison, deposition and post deposition purification experiments were also carried out with tetraethylorthosilicate (TEOS), a precursor that has been used ins CVD[28,29] as well as in FEBID.[31,32]

Scanning electron microscope (SEM) and 3D atomic force microscope (AFM) images of FEBID pads created with TKDMAS are shown in figure 5(a) and (b), respectively, along with the respective AFM cross sections and EDX spectra. These are shown for the direct deposits and for the deposits after post treatment through electron irradiation under water vapour. Table 3 compares the elemental composition before and after post-treatment, as evaluated from the corresponding EDX spectra. The quantitative analysis of the EDX spectrum is done by the software "AZtech" developed by Oxford Instruments, which applies standardless-analysis methodology[53] to determine the elemental composition from an EDX spectrum. For TKDMAS, the untreated deposit composition was 58.6 at% C, 23.5 at% O, 9.4 at% N, and 8.5 at% Si. After post deposition treatment, the composition was 40.6 at% C, 34.5 at% O, 13.6 at% N, and 11.3 at% Si. Hence, for TKDMAS significant reduction in both the relative carbon and nitrogen content is clear. On the other hand, the oxygen content increases, which is likely to be due to partial oxidation of the silicon, as has been observed previously.[54] However, despite efficient carbon and nitrogen removal, only 25 % thickness reduction is observed, as shown in figure 5. Post-treatment of TKDMAS with electron irradiation alone (not shown in figure. 5) did not result in any significant composition change.

Figures 6(a) and (b) show the corresponding SEM and 3D AFM images of the deposits from TEOS before and after post treatment, along with the respective AFM cross sections. Table 4 compares the respective elemental composition before and after post-treatment evaluated to form the corresponding EDX spectra. The composition of the untreated deposit from TEOS was found to be 49.8 at% C, 34.6 at% O, and 15.6 at% Si. After the post treatment, the composition was found to be 45.5 at% C, 38.5 at% O, and 16 at% Si. Hence, no significant composition change was observed after post-treatment of the TEOS deposits, neither in the presence of water nor by electron irradiation alone. The morphology change can be seen from the appearance of the TEOS and TKDMAS FEBID pads after and before post treatment in the AFM and SEM images. In SEM images, due to the SEM edge effect, edges and corners tend to appear brighter. As a result, in the case of presented TEOS and TKDMAS deposits, the outer parts and the edges reveal a brighter appearance than the centers. After post-treatment, the reduced dark centers in both pad types point towards a lower carbon concentration. Furthermore, humps are visible in the AFM and SEM images next to the TKDMAS pads after post treatment. Such post treatment-induced changes are only visible in TKDMAS pads, for which thickness reduction is detected and more pronounced carbon removal can be observed.

For comparison with the DI data, it is reasonable to look at the Si:N ratio as the oxygen and carbon may, in part, originate from background gas present under HV conditions. From these, the main carbon component that is not from the compound will stem from pump oil residues in the chamber. At the same time, the oxygen is likely to be mostly due to water residues that are the predominant background gas under HV conditions (10^{-6}-10^{-8} mbar)[55].

From the composition, it is clear that the Si:N ratio in the TKDMAS pads is close to 1:1, as compared to the initial 1:4 ratio in the intact precursor molecule, i.e., on average, 3 nitrogen atoms are lost from each precursor molecule in the deposition process. In the DI process, in the gas phase, we find an average nitrogen loss per incident of <1.5, which correlates to an expected Si:N deposit ratio of < 1:2.5. Thus, though DI is likely to be the initial step, other processes determine the final composition.

 This journal is © The Royal Society of Chemistry 20xx

Please do not adjust margins

Please do not adjust margins

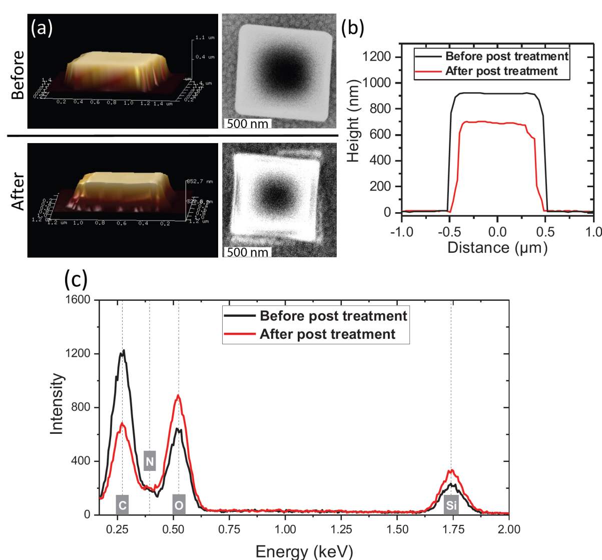

Figure 5. Characterization of FEBID pads deposited by precursor TKDMAS with/without post-treatment with electron irradiation and water vapor. (a) AFM image(left) and SEM image (right), (b) cross-sections extracted from AFM images, (c) EDX spectrum.

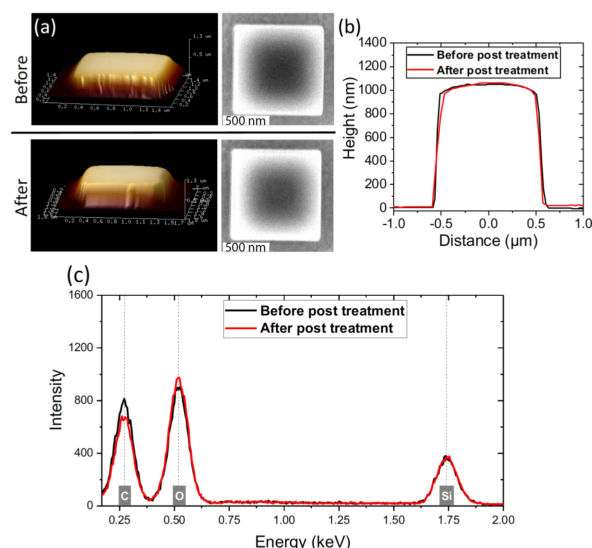

Figure 6. Characterization of FEBID pads deposited by precursor tetraethyl orthosilicate (TEOS) with/without post-treatment with electron irradiation. (a) AFM image(left) and SEM image (right), (b) cross-sections extracted from AFM images, (c) EDX spectrum.

With a TKDMAS diameter of about 6 Å and dense packing, a 1 μm^2 monolayer consist of about 3 × 10^6 molecules, and a 900 nm high pad would contain a total of about 4.5 × 10^9 molecules. Let's take as an example the whole dissociative ionization cross section of ethylene at 5 kV. That is on the order of 10^{-17} cm^2,[56] and coverage of 3 × 10^6 molecules for a 1 μm^2 monolayer. The reactive coverage, calculated as the dissociative ionization cross section times the number of molecules in one monolayer, is about 3 × 10^{-3} μm^2. The total primary electron dose is about 2.5 × 10^{14} $e^-/\mu m^2$, and the exposure of a monolayer is accordingly about 1.5 × 10^{11} $e^-/\mu m^2$. Thus, statistically, 150 DI incidents per molecule (and its resulting fragments) may be expected if the DI cross section is assumed to stay the same after each incident. At 5 k eV primary electron energy, the secondary electron yield is expected to be < 2 per primary electron[57,58] and these will also contribute to DI events. In these back-of-the-envelope calculations, we use gas phase cross section and consider these to remain unchanged for the immobilized fragment(s) resulting from a previous event(s). This does evidently not hold, but it is still clear from these considerations that multiple reactive incidents with the same molecule or its fragments after an initial dissociative ionisation event may occur. This may partly explain the significantly lower N content of the deposits compared to what should be expected from the DI experiments conducted under single collision conditions.

Table 3. elemental composition of FEBIDs created with precursor TKDMAS before and after post-treatment

Element (At %)	C	O	Si	N
Before post treatment	58.6	23.5	9.4	8.5
After post treatment	40.6	34.5	13.6	11.3

However, water is the predominant background gas under HV conditions. At pressures of about 10^{-7} mbar and assuming a sticking coefficient of about 0.2, an equivalent of one monolayer water absorbs on the surface in less than two minutes.[59] Post and in situ treatment with water during electron irradiation has been shown to be effective in the deposition of $(EtCp)_2Ru$ and $MeCpPtMe_3$.[60,61] And in a recent comparative study on FEBID deposition of $Pt(CO)_2Cl_2$ and $Pt(CO)_2Br_2$ under HV and UHV conditions,[62] the HV deposits were found to be as good as free of the halogen component while this was the dominant ligand residue in the UHV experiment. We consider this to be an effect that is due to HCl and HBr formation and desorption through reactions with the residual water in the HV experiment. A similar effects has been observed in electron induced decomposition of $Pt(NH_3)_2Cl_2$ and $(\eta^3\text{-}C_3H_5)Ru(CO)_3Cl$ [63,64] In the former case, reductive HCl formation takes place through intramolecular reactions of the halogen with hydrogen from the amino ligand in the latter case by in situ exposure to ammonia in the electron irradiation process.

From the oxygen content of the initial deposit, it is evident that in the extended application of TKDMAS for FEBID, the presence of trace water is determined for the resulting composition, not only through oxide formation in the remaining deposit but also through the removal of carbon and nitrogen. Due to the absence of nitrogen

Table 4. elemental composition of FEBIDS created with precursor TEOS before and after post-treatment

Element (At %)	C	O	Si
Before post treatment	49.8	34.6	15.6
After post treatment	45.5	38.5	16

Please do not adjust margins

Please do not adjust margins

in TEOS, FEBIDs with these two precursors may be worth pursuing as a path for composition control in silicon nitride and silicon oxynitride deposits. Control of the partial water pressures during the deposition process might also offer a path for optimizing such deposits, particularly from TKDMAS. Controlled UHV experiments would be valuable in this context to evaluate the nature of the desorbing fragments (MS) and the chemical bonding in the deposit (XPS) at controlled water vapour pressures as the base water pressure is very low in such instruments.

Conclusions

Here we presented a combined experimental and theoretical study on dissociative ionization of TKDMAS and compared the extent of the fragmentation observed with the composition of deposits formed with this compound in FEBID before and after post-treatment by electron irradiation in the presence of water. In DI, the fragmentation of TKDMAS is characterized by the loss of $N(CH_3)_2$ units. Simple direct cleavage of the Si-$N(CH_3)_2$ bond is, however, only observed for the loss of one $N(CH_3)_2$ moiety. All other fragmentation channels are associated with rearrangement reactions, mainly hydrogen transfer and new N-N bond formation leading to the respective methyl hydrazine derivatives. The average nitrogen loss from TKDMAS per DI incident under a single collision condition in the gas phase is found to be < 1.5. The Si:N ratio in the FEBID, however, is found to be close to 1:1, which translates to an average loss of three nitrogen from each molecule in the deposition process. This is more than two times what would be expected from the gas phase experiments. Ex-situ post treatment through further electron exposure in the presence of water further increases the Si:N ratio slightly. For TKDMAS, we believe that the presence of water traces during the deposition process under HV conditions is determined for the resulting composition. It is clear from the current study that the composition may be further tuned in post treatment with water under electron irradiation. This may offer a route for controlled silicon oxynitride deposition in FEBID by controlled water admission in the deposition process. UHV surface experiments, where the desorbing fragments and the bonding nature within the deposit can be monitored, would be a valuable extension of this study. Especially as the residual gas under UHV is mainly CO and hydrogen, and water admission during electron exposure can thus be well controlled.

Author Contributions

Po-Yuan Shih and Reza Tafrishi had Equal First author contribution in writing (review & editing) the article.

Conflicts of interest

“There are no conflicts to declare”.

Acknowledgements

This project has received funding from the European Union’s Horizon 2020 research and innovation programme under the Marie Skłodowska-Curie grant agreement No 722149. M.C. and O.I. acknowledge support from the Icelandic Centre of Research (RANNIS), grant no. 13049305(1–3). MC acknowledges a doctoral grant from the University of Iceland Research Fund.

References

1 W. Kern and R. S. Rosler, in *J Vac Sci Technol*, 1977, vol. 14, pp. 1082–1099.

2 A. K. Sinha, H. J. Levinstein, T. E. Smith, G. Quintana and S. E. Haszko, Reactive Plasma Deposited Si-N Films for MOS-LSI Passivation, *J. Electrochem. Soc.*, 1978, **125**, 601–608.

3 H. Sato, A. Izumi, A. Masuda and H. Matsumura, *Low-k silicon nitride film for copper interconnects process prepared by catalytic chemical vapor deposition method at low temperature*, 2001, vol. 395.

4 R. Blanc, F. Leverd, M. Darnon, G. Cunge, S. David and O. Joubert, Patterning of silicon nitride for CMOS gate spacer technology. III. Investigation of synchronously pulsed CH 3 F/O 2 /He plasmas , *J. Vac. Sci. Technol. B, Nanotechnol. Microelectron. Mater. Process. Meas. Phenom.*, 2014, **32**, 021807.

5 Nishi; Y.; Doering; R.T; Eds., Handbook of semiconductor manufacturing technology (2nd ed.), *CRC Press,* 2008.

6 Y. Wang, X. Cheng, Z. Lin, C. Zhang and F. Zhang, Optimization of PECVD silicon oxynitride films for anti-reflection coating, *Vacuum*, 2003, **72**, 345–349.

7 Y. Shi, L. He, F. Guang, L. Li, Z. Xin and R. Liu, A review: Preparation, performance, and applications of silicon oxynitride film, *Micromachines*, 2019, **10**, 1–23.

8 J. E. Crowell, Chemical methods of thin film deposition: Chemical vapor deposition, atomic layer deposition, and related technologies, *J. Vac. Sci. Technol. A Vacuum, Surfaces, Film.*, 2003, **21**, S88–S95.

9 O. Sneh, R. B. Clark-Phelps, A. R. Londergan, J. Winkler and T. E. Seidel, Thin film atomic layer deposition equipment for semiconductor processing, *Thin Solid Films*, 2002, **402**, 248–261.

10 J. M. De Teresa, A. Fernández-Pacheco, R. Córdoba, L. Serrano-Ramón, S. Sangiao and M. R. Ibarra, Review of magnetic nanostructures grown by focused electron beam induced deposition (FEBID), *J. Phys. D. Appl. Phys.*, 2009, **42**, DOI:10.1088/0022-3727/49/24/243003.

11 I. Utke, P. Hoffmann and J. Melngailis, Gas-assisted focused electron beam and ion beam processing and fabrication, *J. Vac. Sci. Technol. B Microelectron. Nanom. Struct.*, 2008, **26**, 1197.

12 W. F. Van Dorp and C. W. Hagen, A critical literature review of focused electron beam induced deposition, *J. Appl. Phys.*, 2008, **104**, DOI:10.1063/1.2977587.

13 M. Huth, F. Porrati, C. Schwalb, M. Winhold, R. Sachser, M. Dukic, J. Adams and G. Fantner, Focused electron beam

This journal is © The Royal Society of Chemistry 20xx

Please do not adjust margins

Please do not adjust margins

induced deposition: A perspective, *Beilstein J. Nanotechnol.*, 2012, **3**, 597–619.

14 H. Plank, R. Winkler, C. H. Schwalb, J. Hütner, J. D. Fowlkes, P. D. Rack, I. Utke and M. Huth, Focused electron beam-based 3D nanoprinting for scanning probe microscopy: A review,*Micromachines*, 2020,**11**, DOI:10.3390/mi11010048

15 T. Maruyama and T. Shirai, Silicon dioxide thin films prepared by chemical vapor deposition from tetrakis (dimethylamino)silane and ozone, *Appl. Phys. Lett.*, 1993, **63**, 611–613.

16 B. B. Burton, S. W. Rang, S. W. Rhee and S. M. George, Sic 2 atomic layer deposition using tris(dimethylamino)silane and hydrogen peroxide studied by in situ Transmission FTIR spectroscopy, *J. Phys. Chem. C*, 2009, **113**, 8249–8257.

17 T. Bret, T. Hofmann and K. Edinger, Industrial perspective on focused electron beam-induced processes, *Appl. Phys. A Mater. Sci. Process.*, 2014, **117**, 1607–1614.

18 I. Utke, P. Hoffmann and J. Melngailis, Gas-assisted focused electron beam and ion beam processing and fabrication, *J. Vac. Sci. Technol. B Microelectron. Nanom. Struct.*, 2008, **26**, 1197.

19 S. Heterojunctions, N. Tohge, T. Minami and M. Tanaka, *Characterization and Application of Materials Grown by Electron-Beam-Induced Deposition Related content Electron-Beam-Induced Current in Amorphous Chalcogenide Film/Crystalline*, 1994, vol. 33.

20 S. J. Randolph, J. D. Fowlkes and P. D. Rack, Focused, nanoscale electron-beam-induced deposition and etching, *Crit. Rev. Solid State Mater. Sci.*, 2006, **31**, 55–89.

21 N. Silvis-Cividjian, C. W. Hagen, L. H. A. Leunissen and P. Kruit, *The role of secondary electrons in electron-beam-induced-deposition spatial resolution*, 2002.

22 A. Botman, D. A. M. de Winter and J. J. L. Mulders, Electron-beam-induced deposition of platinum at low landing energies, *J. Vac. Sci. Technol. B Microelectron. Nanom. Struct.*, 2008, **26**, 2460–2463.

23 J. Schaefer, J. Hoelzl, Y. Tian, T. Zhou, B. Zhang, Y. Jin and H. Jiang, A contribution to the dependence of secondary electron emission from the work function and fermi energy, *J. Phys. D. Appl. Phys.*, 1972, **31**, 81–86.

24 K. Ohya, A. Harada, J. Kawata and K. Nishimura, Monte Carlo simulation of yield and energy distribution of secondary electrons emitted from metal surfaces, *Japanese J. Appl. Physics, Part 1 Regul. Pap. Short Notes Rev. Pap.*, 1996, **35**, 6226–6232.

25 R. M. Thorman, T. P. Ragesh Kumar, D. Howard Fairbrother and O. Ingólfsson, The role of low-energy electrons in focused electron beam induced deposition: Four case studies of representative precursors, *Beilstein J. Nanotechnol.*, 2015, **6**, 1904–1926.

26 S. L. Toh, T. E. Tay, P. Examiner and K. M. Picardat, Method to improve adhesion of dielectric films in damascene interconnects, *US Pat, 2004.*

27 G. Spencer, A. Soyemi, K. Junker, J. Vires, M. Turner, S. Kirksey, D. Sieloff and N. Ramani, Optimization of dielectric cap adhesion to ultra-low-k dielectrics, *Mater. Res. Soc. Symp. Proc.*, 2004, **812**, 117–122.

28 K. H. A. Bogart, S. K. Ramirez, L. A. Gonzales, G. R. Bogart and E. R. Fisher, Deposition of SiO2 films from novel alkoxysilane/O2 plasmas, *J. Vac. Sci. Technol. A Vacuum, Surfaces, Film.*, 1998, **16**, 3175–3184.

29 F. Fracassi and R. D'Agostino, Plasma deposition of silicon nitride-like thin films from organosilicon precursors, *Plasmas Polym.*, 1996, **1**, 3–16.

30 M. Adachi, K. Okuyama and T. Fujimoto, Film formation by a new chemical vapor deposition process using ionization of tetraethylorthosilicate, *Jpn. J. Appl. Phys.*, 1995, **34**, L1148–L1150.

31 T. Bret, I. Utke, A. Bachmann and P. Hoffmann, In situ control of the focused-electron-beam-induced deposition process, *Appl. Phys. Lett.*, 2003, **83**, 4005–4007.

32 S. Frabboni, G. C. Gazzadi and A. Spessot, Transmission electron microscopy characterization and sculpting of sub-1 nm Si-O-C freestanding nanowires grown by electron beam induced deposition, *Appl. Phys. Lett.*, 2006, **89**, 1–4.

33 E. H. Bjarnason, B. Ómarsson, S. Engmann, F. H. Ómarsson and O. Ingólfsson, Dissociative electron attachment to titatinum tetrachloride and titanium tetraisopropoxide, *Eur. Phys. J. D*, 2014, **68**, DOI:10.1140/epjd/e2014-50091-9.

34 F. Neese, Software update: the ORCA program system, version 4.0, *Wiley Interdiscip. Rev. Comput. Mol. Sci.*, 2012, **2** , DOI:10.1002/wcms.1327.

35 C. Adamo and V. Barone, Toward reliable density functional methods without adjustable parameters: The PBE0 model, *J. Chem. Phys.*, 1999, **110**, 6158–6170.

36 F. Weigend and R. Ahlrichs, Balanced basis sets of split valence, triple zeta valence and quadruple zeta valence quality for H to Rn: Design and assessment of accuracy, *Phys. Chem. Chem. Phys.*, 2005, **7**, 3297–3305.

37 S. Grimme, J. Antony, S. Ehrlich and H. Krieg, A consistent and accurate ab initio parametrization of density functional dispersion correction (DFT-D) for the 94 elements H-Pu, *J. Chem. Phys.*, 2010, **132**, DOI:10.1063/1.3382344.

38 C. Riplinger and F. Neese, An efficient and near linear scaling pair natural orbital based local coupled cluster method, *J. Chem. Phys.*, 2013,**138**, DOI:10.1063/1.4773581

39 C. Riplinger, P. Pinski, U. Becker, E. F. Valeev and F. Neese, Sparse maps - A systematic infrastructure for reduced-scaling electronic structure methods. II. Linear scaling domain based pair natural orbital coupled cluster theory, *J. Chem. Phys.*, 2016, **144**, DOI:10.1063/1.4939030.

40 C. Riplinger, B. Sandhoefer, A. Hansen and F. Neese, Natural triple excitations in local coupled cluster calculations with pair natural orbitals, *J. Chem. Phys.*, 2013, **139** , DOI:10.1063/1.4821834.

41 A. Hellweg, C. Hättig, S. Höfener and W. Klopper, Optimized accurate auxiliary basis sets for RI-MP2 and RI-CC2 calculations for the atoms Rb to Rn, *Theor. Chem. Acc.*, 2007, **117**, 587–597.

42 D. H. Aue, H. M. Webb, W. R. Davidson, M. Vidal, M. T. Bowers, H. Goldwhite, L. E. Vertal, J. E. Douglas, P. A. Kollman and G. L. Kenyon, Proton Affinities and Photoelectron Spectra of Three-Membered-Ring Heterocycles, *J. Am. Chem. Soc.*, 1980, **102**, 5151–5157.

Please do not adjust margins

Please do not adjust margins

43 J. C. Traeger, Gas-phase heats of formation for alkylimmonium cations by photoionization mass spectrometry, *J. Phys. Chem. A*, 2007, **111**, 4643–4649.

44 A. Bodi, B. Sztáray and T. Baer, Dissociative photoionization of mono-, di- and trimethylamine studied by a combined threshold photoelectron photoion coincidence spectroscopy and computational approach, *Phys. Chem. Chem. Phys.*, 2006, **8**, 613–623.

45 R. M. Thorman, I. Unlu, K. Johnson, R. Bjornsson, L. McElwee-White, D. H. Fairbrother and O. Ingólfsson, Low energy electron-induced decomposition of (η5-Cp)Fe(CO)2Mn(CO)5, a potential bimetallic precursor for focused electron beam induced deposition of alloy structures, *Phys. Chem. Chem. Phys.*, 2018, **20**, 5644–5656.

46 R. M. Thorman, S. J. Matsuda, L. McElwee-White and D. H. Fairbrother, Identifying and Rationalizing the Differing Surface Reactions of Low-Energy Electrons and Ions with an Organometallic Precursor, *J. Phys. Chem. Lett.*, 2020, **11**, 2006–2013.

47 R. M. Thorman, P. A. Jensen, J.-C. Yu, S. J. Matsuda, L. McElwee-White, O. Ingólfsson and D. H. Fairbrother, Electron-Induced Reactions of Ru(CO) 4 I 2 : Gas Phase, Surface, and Electron Beam-Induced Deposition , *J. Phys. Chem. C*, 2020, **124**, 10593–10604.

48 E. Bilgilisoy, R. M. Thorman, J. C. Yu, T. B. Dunn, H. Marbach, L. McElwee-White and D. H. Fairbrother, Surface Reactions of Low-Energy Argon Ions with Organometallic Precursors, *J. Phys. Chem. C*, 2020, **124**, 24795–24808.

49 K. Landheer, S. G. Rosenberg, L. Bernau, P. Swiderek, I. Utke, C. W. Hagen and D. H. Fairbrother, Low-energy electron-induced decomposition and reactions of adsorbed tetrakis(trifluorophosphine)platinum [Pt(PF3)4], *J. Phys. Chem. C*, 2011, **115**, 17452–17463.

50 J. A. Spencer, Y. C. Wu, L. McElwee-White and D. H. Fairbrother, Electron Induced Surface Reactions of cis-Pt(CO)2Cl2: A Route to Focused Electron Beam Induced Deposition of Pure Pt Nanostructures, *J. Am. Chem. Soc.*, 2016, **138**, 9172–9182.

51 M. Zlatar, M. Allan and J. Fedor, Excited states of Pt(PF3)4 and their role in focused electron beam nanofabrication, *J. Phys. Chem. C*, 2016, **120**, 10667–10674.

52 M. Allan, Electron scattering in Pt(PF3)4: Elastic scattering, vibrational, and electronic excitation, *J. Chem. Phys.*, 2011, **134**, DOI:10.1063/1.3594206.

53 S. Burgess, What is Standardless Quantitative Analysis_ - Nanoanalysis - Oxford Instruments, https://nano.oxinst.com/library/blog/what-is-standardless-quantitative-analysis.

54 T. P. Ragesh Kumar, S. Hari, K. K. Damodaran, O. Ingólfsson and C. W. Hagen, Electron beam induced deposition of silacyclohexane and dichlorosilacyclohexane: The role of dissociative ionization and dissociative electron attachment in the deposition process, *Beilstein J. Nanotechnol.*, 2017, **8**, 2376–2388.

55 S. Abdel-Samad, M. Abdel-Bary and K. Kilian, Residual gas analysis in the TOF vacuum system, *Vacuum*, 2005, **78**, 83–89.

56 R. Kumar and P. K. Sharma, Electron impact ionization cross sections of C2H4 molecule, *Chem. Phys. Impact*, 2020, **1**, 100004.

57 P. Lundgreen, M.Sc thesis, 2020.

58 K. Tuğrul ARAT, Ph.D thesis, 2021.

59 N. B. F. Hall, MatSci 571 : Molecules on Surfaces Molecules on Surfaces, www.wsu.edu/~hipps/M571.htm, 2014.

60 M. Rohdenburg, R. Winkler, D. Kuhness, H. Plank and P. Swiderek, Water-Assisted Process for Purification of Ruthenium Nanomaterial Fabricated by Electron Beam Induced Deposition, *ACS Appl. Nano Mater.*, 2020, **3**, 8352–8364.

61 Z. Warneke, M. Rohdenburg, J. Warneke, J. Kopyra and P. Swiderek, Electron-driven and thermal chemistry during water-assisted purification of platinum nanomaterials generated by electron beam induced deposition, *Beilstein J. Nanotechnol.*, 2018, **9**, 77–90.

62 A. Mahgoub, H. Lu, R. M. Thorman, K. Preradovic, T. Jurca, L. McElwee-White, H. Fairbrother and C. W. Hagen, Electron beam-induced deposition of platinum from Pt(CO)2Cl2 and Pt(CO)2Br2, *Beilstein J. Nanotechnol.*, 2020, **11**, 1789–1800.

63 J. Warneke, M. Rohdenburg, Y. Zhang, J. Orzagh, A. Vaz, I. Utke, J. T. M. De Hosson, W. F. Van Dorp and P. Swiderek, Role of NH3 in the Electron-Induced Reactions of Adsorbed and Solid Cisplatin, *J. Phys. Chem. C*, 2016, **120**, 4112–4120.

64 M. Rohdenburg, H. Boeckers, C. R. Brewer, L. McElwee-White and P. Swiderek, Efficient NH3-based process to remove chlorine from electron beam deposited ruthenium produced from (η3-C3H5)Ru(CO)3Cl, *Sci. Rep.*, 2020, **10**, 1–13.

This journal is © The Royal Society of Chemistry 20xx

Please do not adjust margins